22nd International Conference on Sustainable Energy Technologies
Kuala Lumpur, Malaysia, 13 to 15 August 2026 · ISBN 978-1-995850-00-9 · ISSN 2978-4387

CONFERENCE PAPER · ENERGY STORAGE & CONVERSION

Experimental energy analysis of a trigeneration system based on outdoor air temperature: a case study at Fatsa State Hospital, Türkiye

Ali Kilicarslan[1*], Engin Sanli[2]

[1] Hitit University, Faculty of Engineering and Natural Sciences, Department of Mechanical Engineering, 19030 Çevreyolu, Çorum, Türkiye

[2] Hitit University, Construction Works Department, 19030 Çevreyolu, Çorum, Türkiye

RECEIVED 11 February 2026 · REVISED 14 March 2026 · ACCEPTED 23 March 2026
PRESENTED 13 to 15 August 2026 · PUBLISHED 23 November 2026

ABSTRACT

In addition to electricity generation, trigeneration systems produce cooling energy from waste heat for air conditioning in summer and heating energy to meet part of the heating needs of spaces in winter. Because they recover waste energy, the use of trigeneration systems is increasing, especially in central heating systems and government buildings. Because waste heat is recovered, less energy is used, carbon emissions are reduced, and, consequently, trigeneration systems significantly mitigate global warming. In this real-time case study, temperature, pressure, relative humidity, and flow rate were measured from the trigeneration system of Fatsa State Hospital during the winter months at varying outdoor air temperatures. The changes in the amount of electricity and heat energy produced by the trigeneration system's gas engine, the air and fuel flow rate entering the gas engine, the air-fuel ratio, the relative humidity of the air, the engine's thermal capacity, capacity of high temperature heat exchanger (HET), capacity of hot water heat exchanger (HWE) and the engine's mechanical and thermal efficiencies were investigated at outside air temperatures ranging from 10 °C to 20 °C. For this purpose, a computer program was developed using EES (Engineering Equation Solver) software. It was observed that the heat power generated by the trigeneration system ranged from 427.1 kW to 433.2 kW, while the electrical power remained constant at 400 kW. Based on these powers, the average thermal and electrical efficiencies were 41% and 44%, respectively. Due to the increase in outside air temperature, the density of natural gas decreased, resulting in a reduction in the total heating value of the fuel from 997.8 kW to 954.5 kW.

KEYWORDS Trigeneration system, Gas engine, Electricity generation, Heat recovery

1. Introduction

Energy is used in many areas of our daily lives. Heating is one of the most important of these areas. Our heating needs are met either by conventional systems where the heat produced is distributed through pipes, or by newer, more efficient heating systems such as heat pumps, trigeneration, and cogeneration.

Therefore, it is necessary to increase the amount of useful energy, which is the portion of energy that is used, and to promote the use of different environmentally friendly energy production systems. Among these systems, the first that come to mind are combined heat-power-cooling (CHP) systems, which are becoming increasingly common in our country, as well as cogeneration and trigeneration systems. Cogeneration systems convert fuel energy input into both electrical and thermal energy outputs. Trigeneration systems, on the other hand, can also provide cooling in addition to the electrical and thermal energy they produce.

* Corresponding author. Email address: alikilicarslan@hitit.edu.tr (Ali Kilicarslan)

© 2026 The Author(s).
Published by Caravel Press.

doi.org/10.65582/set.2026.005

Cogeneration and trigeneration systems are becoming increasingly widespread in universities, hospitals, shopping malls, and many industrial sectors. Literature research reveals that numerous studies have been conducted on trigeneration and cogeneration systems.

Santiago *et al.* (2022) conducted a thermodynamic analysis and optimization of a trigeneration system for four different configurations in a medium-sized hospital. Their study found that the best trigeneration configuration was an integrated organic Rankine cycle system, with an energy efficiency of approximately 81% and an exergy efficiency of approximately 42%. Cavalcanti (2021) investigated two different trigeneration systems, one diesel and one gas-diesel, based on their energy and exergy efficiencies and environmental impact rates. From the diesel-fueled trigeneration system, they calculated 6.90 MW of electrical power, 28.16 kW of cooling water, and heating capacities of 278.2 and 588 kW. Alcântara *et al.* (2019) investigated the exergy and payback period of a gas-powered, heat recovery, absorption-cooled trigeneration system for an ice cream factory. They determined that the trigeneration system, intended to meet the factory's electricity needs, would require 214.1 kW, 35.7 kW, and 162.1 kW of electricity, heating, and cooling, respectively, when the engine is operating at 100% capacity (full load).

Kaplan and Büker (2019) conducted research on the applicability of a packaged micro-cogeneration system with a capacity of 71 kW of electricity and 115 kW of heat, which was commissioned in Konya in 2016 and implemented for the first time in a residential project in Türkiye. They determined that this system produced 2.64 units of electricity for every unit of natural gas consumed on average per month. They found that the system should operate for at least 4500 hours/year without entering sleep mode and should not exceed 15% of the previously determined building heating requirement. They observed that the selected device generated 30.54 kW of electricity per hour in summer and 48 kW per hour in winter. They determined that the electricity produced by the device reduced electricity consumption by 51%. Based on data obtained from the system's operation over a certain period, they determined the device's thermal efficiency to be 87%.

Shelar *et al.* (2016) conducted a thermodynamic analysis of a 200 kW diesel engine-powered trigeneration system and examined two different trigeneration systems, one with a single-effect and one with a double-effect absorption chiller, using the same temperature conditions. In this context, they performed energy and exergy analyses of two predetermined systems in cooling mode. They found that although the investment cost of the double-effect absorption chiller was higher than that of the single-effect absorption chiller, it was more attractive because of its shorter payback period.

Üçgül and Elibüyük (2015) conducted a study on the feasibility of a trigeneration system for Süleyman Demirel University, investigating a natural gas-fueled trigeneration system that could meet the energy needs of the university campus, including electricity, cooling, and heating. The study determined that the system's operating costs were 7,537,897 TL, the system's revenue was 9,661,364 TL, and the payback period was 25 months.

Ziher and Poredos (2006), in their study comparing trigeneration and cogeneration systems from an economic perspective, found that trigeneration systems had a higher initial investment cost. Still, the payback period was 6.71 years for cogeneration and 5.86 years for trigeneration.

Salem Szklo *et al.* (2004) first investigated hospital energy consumption in Brazil and examined the costs of obtaining electricity, heating, and cooling energy from trigeneration systems in the healthcare sector. They concluded that motor turbines and chillers should be selected for heating and cooling according to electricity needs.

In their study, Luz-Silveira *et al.* (2002) conducted a thermo-economic analysis of a cogeneration plant on a university campus with an electricity demand of 9 MW. They found that by operating a 3 MW electric generator in a gas turbine cogeneration system with a 10-year payback period, they met approximately one-third of the university's electricity needs.

A literature review shows that far fewer studies involve experimental and applied research than theoretical work.

To fill this gap, this study will analyze the energy performance of a trigeneration system installed at Fatsa State Hospital by collecting temperature, pressure, flow rate, and related data from specific operating points under different outside air temperatures. Within the scope of this study, a computer program will be developed using EES software (Klein 2020), commonly used for thermodynamic analysis of thermal systems, to determine the generated electrical and thermal power, heat exchanger thermal capacity values, and electrical and thermal efficiencies according to the outside air temperature.

2. Materials and Method

The 800 kWe gas engine absorption-cooled trigeneration system examined in this study was established in 2015 to support the electrical, heating, and cooling loads of the 300-bed Fatsa State Hospital and was commissioned in September 2019. The hospital is located in Fatsa district of Ordu province in Türkiye. The hospital complex, built on a 27,433 m² covered area, has a total covered area of 47,784 m². The hospital building entrance faces the Black Sea and is oriented towards the northeast.

As shown in Figure 1, to the right of the entrance of Fatsa State Hospital, there is a two-story heating and energy center building with a closed area of 827 m², which meets the heating and electricity needs of the building and its campus (Sanli 2022).

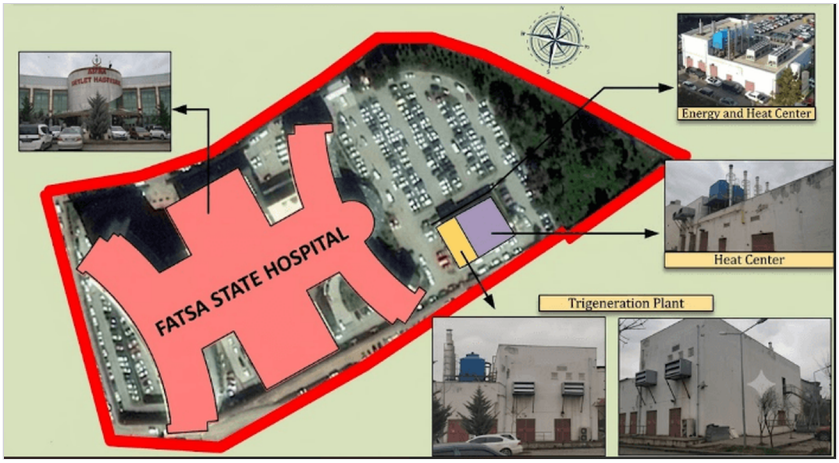

Figure 1. Layout and representation of Fatsa State Hospital, trigeneration and heating center buildings.

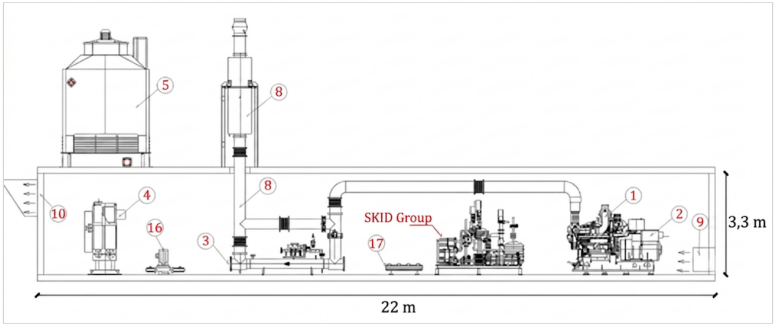

Figure 2. Schematic side view of the trigeneration system (Sanli 2022).

Figure 2 shows a side view of the trigeneration system, and Figure 3 shows a top view of the trigeneration system. Table 1 below lists the key equipment components within a trigeneration system, including their brand, model, quantity, and power rating.

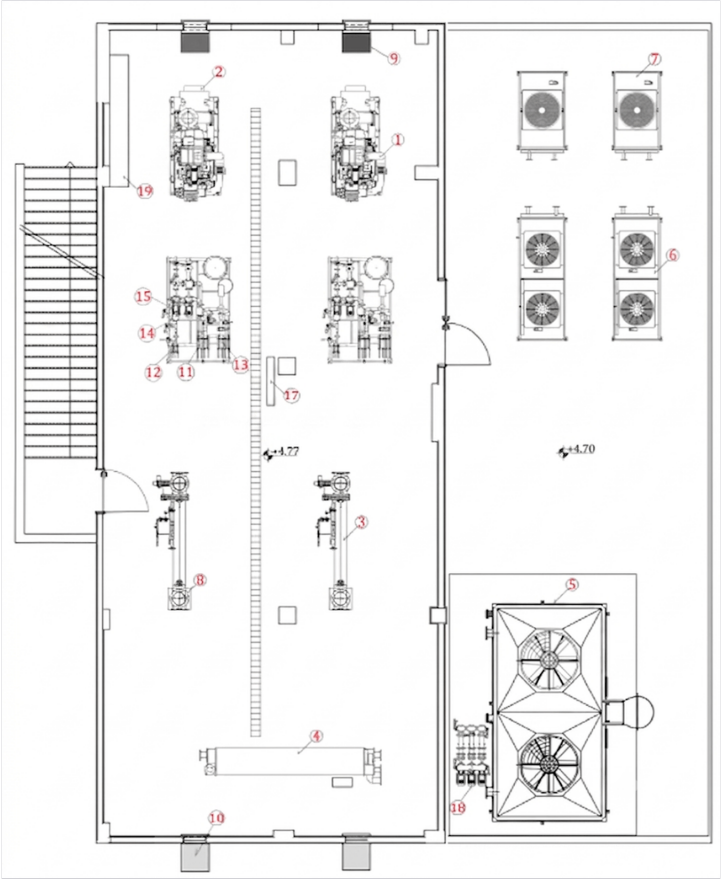

Figure 3. Schematic top view of the trigeneration system (Sanli 2022).

Table 1. List of devices and equipment for trigeneration systems (Sanli 2022).

Number	Quantity	Equipment Name	Brand Name	Model	Power
1	2	Internal combustion gas engine	Caterpillar	CG132-8	0.400 MWe
2	2	Generator	Marelli	MJB 355 MB 4	0.400 MWe
3	2	Heat recovery system	Aprovis	-	227 kW
4	1	Absorption Chiller	Broad	BDH	600 kW
5	1	Cooling tower	Yol Yapı	DSKC-9CP	1494 kW
6	2	HT Radiator	Friterm	FDH 2E 8012	283.5 kW
7	2	LT Radiator	Friterm	FDH 2E 9111	32.2 kW
8	2	Chimney	Meba	Ø350	-
9	2	Supply fan	Pitsan	PV900	2500 m^3/h, 30 mWG

Table 1. (continued)

Number	Quantity	Equipment Name		Brand Name	Model	Power
10	2	Return fan		Pitsan	PV900	2300 m³/h, 30 mWG
11	2	HTE	SKID UNIT	Alfa Laval	M6-FM	204 kW
12	2	LTE		Alfa Laval	M3-FG	25 kW
13	2	HWE H.Exchanger		Alfa Laval	M6-MFM	431 kW
14	2	HT Pump		Grundfoss	NB 32-125/130	24 m³/h, 20 mWG
15	2	LT Pump		Grundfoss	NB 32-125.1/133	8 m³/h, 24 mWG
16	2	HWE Pump Return		Grundfoss	NB 32-	47 m³/h, 10 mWG
17	1	HWE Pump Return				
18	3	Cooling Tow. Pump		Grundfoss	NB125-315/296 33315/296	259 m³/h, 24.5 mWG
19	2	Control Panel				

The most important components of the trigeneration system, namely the internal combustion gas engines/generators, heat recovery system, absorption chiller (absorption refrigeration system), and SKID unit, are shown in Figure 4.

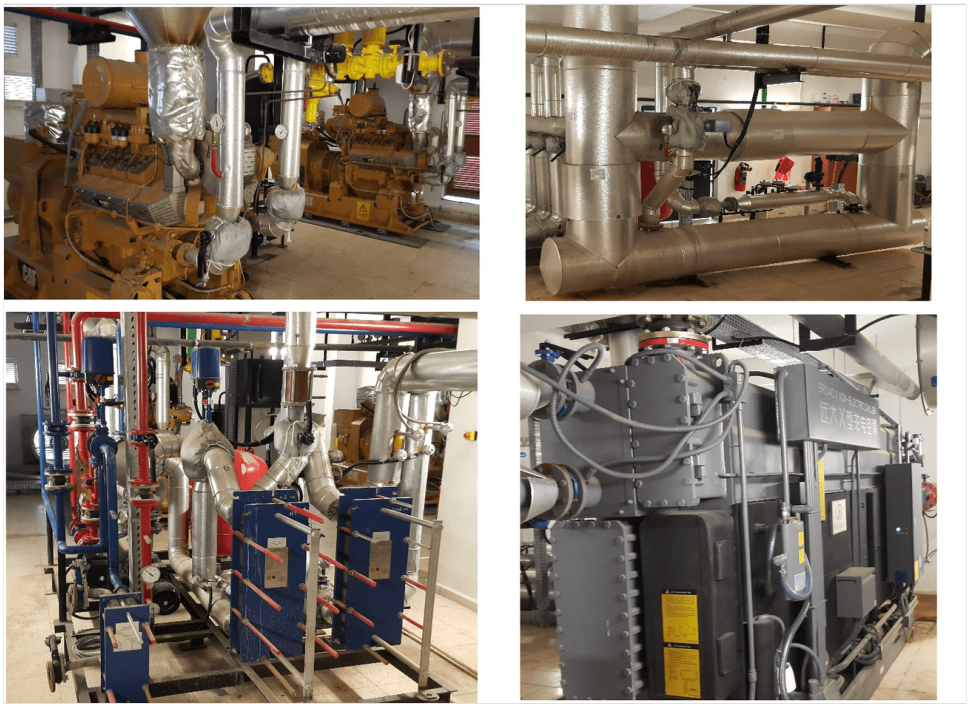

Figure 4. Main elements of trigeneration system a) Internal combustion gas engine and generators b) Heat recovery system c) SKID unit d) Absorption chiller (Sanli 2022).

One of the most important components of a trigeneration system is the gas engine and generator shown in Figure 4a. The heat released from the combustion of fuel in the internal combustion gas

engine is converted into mechanical energy, which then drives the generator via the same shaft, thus generating electricity. Gas engine trigeneration systems are preferred, especially when electricity demand exceeds heat demand, because they can generate electrical energy at low capacities. Furthermore, their quick commissioning and the fact that they contain fewer parts compared to other motor drives make maintenance easier. The heat recovery system (HRS) shown in Figure 4b uses the exhaust waste heat (heating) from the gas engine at high temperatures. The gas engine jacket heat (204 kW) is transferred to a high-temperature heat exchanger (HTE). Water heated to 87 °C by the HTE is sent into the HRS. The HRS contains cylindrical steel tubes to increase the surface area. Exhaust gases entering the boiler at 468 °C transfer their heat to the water, raising its temperature to 95 °C. As a result, the exhaust gases are cooled to 120 °C before being released into the atmosphere. This both adds a heat load of 227 kW to the system and prevents the release of harmful gases into the atmosphere. The SKID Unit shown in Figure 4c contains plate heat exchangers (HTE, LTE, and HWE), pumps (HT, LT, and HW pumps), valves, and other equipment. Figure 4d shows the absorption chiller, also known as the absorption refrigeration unit, a crucial part of the trigeneration system. The trigeneration system uses a Broad brand BDH model absorption refrigeration chiller (ABS) with LiBr-H2O as the single-effect fluid pair. The absorption chiller is designed to provide a chilled water output of 7–12 °C when operating at 95–80 °C. Under these conditions, the cooling load of the unit is 600 kW. Due to its single-effect nature, the ABS chiller is only operated during the summer months. In this study, ABS chillers were not included in the calculations because the energy analysis of the trigeneration system was performed according to winter conditions.

The experimental study was conducted in February at the trigeneration plant located in the heating and energy block of Fatsa State Hospital. Due to winter conditions, the trigeneration system under investigation was operated in heating mode. In heating mode, the system consisted of main equipment (devices) such as a gas engine, heat recovery boiler, plate heat exchangers, low-temperature radiators, and pumps. Additionally, auxiliary components included pipes, valves (3-way, 2-way, etc.), gauges (manometer, thermometer, etc.), manifolds, and filters. Temperature and pressure information from the main equipment operating in heating mode was measured in real time via the system's SCADA screen using mechanical and digital manometers and thermometers (mounted on the system components), and differential pressure gauges measuring the pressure difference between the inlet and outlet lines.

In February 2022, temperature, pressure, flow rate, and other data were measured at specific operating points of the trigeneration system under six different ambient temperatures ranging from 10 °C to 20 °C. All data were collected at least three times under the same ambient temperatures, with the engine operating at the same capacity, for a total of approximately 600 data points. The averages of these data points were used to create average temperature, pressure, and flow rate data for the six different temperature values (10 °C, 12 °C, 14 °C, 16 °C, 18 °C, and 20 °C) at the system's designated operating points.

3. Thermodynamic Analysis

In thermodynamic analysis, the internal combustion gas engine and generator, which are part of electricity and heat production, will be examined together. Then, the heat recovery device, which recovers heat from the generator's exhaust gases, will be investigated.

In the thermodynamic analysis, the conservation equations of mass (Equation 1) and energy (Equation 2) will be analyzed together for the control volume shown below.

$$\frac{dm_{CV}}{dt} = \sum \dot{m}_i - \sum \dot{m}_e \tag{1}$$

$$\frac{dE_{CV}}{dt} = \sum \dot{m}_i \left(h_i + \frac{V_i^2}{2} + gZ_i \right) - \sum \dot{m}_e \left(h_e + \frac{V_e^2}{2} + gZ_e \right) + \dot{Q}_{CV} - \dot{W}_{CV} \quad (2)$$

Where:

- E = energy (kJ)
- $\dot{Q}$ = heat transfer per unit time (kW)
- $\dot{W}$ = work transfer per unit time (kW)
- $\dot{m}_i$ = mass flow rate (kg/s)
- h = specific enthalpy (kJ/kg)
- CV = control volume
- V = velocity (m/s)
- g = gravitational acceleration (m/s²) (9.81 m/s²)
- Z = elevation from the reference point (m)
- i = inlet
- e = exit

The following assumptions apply to both the internal combustion gas engine and generator set, as well as the heat recovery unit.

Steady-state, steady-flow (SSSF) conditions are assumed to be valid through the system.

Changes in kinetic and potential energies are assumed to be negligible.

Ideal gas equations are assumed to apply for air, gas (CH_4), and exhaust gases.

For SSSF, this is because there are no time variations in mass and energy within an open system, and also because changes in kinetic and potential energy are neglected.

$$\sum \dot{m}_i = \sum \dot{m}_e \quad (3)$$

$$\dot{Q}_{CV} - \dot{W}_{CV} = \sum \dot{m}_e h_e - \sum \dot{m}_i h_i \quad (4)$$

3.1. Internal Combustion Gas Engine and Generator

Figure 5 shows the schematic of the internal combustion gas engine and generator set used for the thermodynamic analysis.

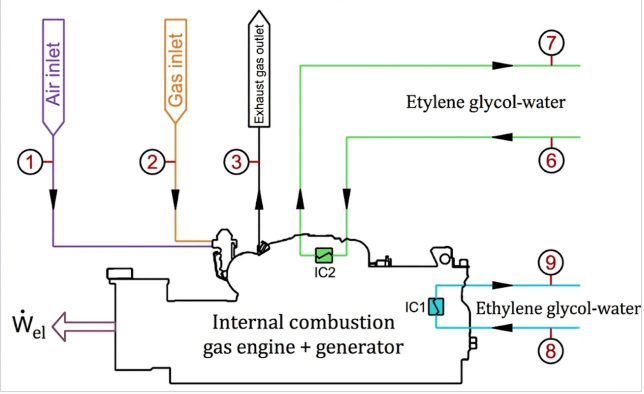

Figure 5. Internal combustion gas engine and generator group.

As shown in Figure 5, air and gaseous fuel (methane) enter through operating points 1 and 2, respectively, and the gases resulting from combustion exit through operating point 3 and go to the

heat recovery system. At operating point 8, an ethylene glycol-water mixture enters the engine to cool the jackets of the internal combustion gas engine (IC1). The ethylene glycol-water mixture is activated only at operating point 6 in very urgent situations; in other words, when the heat load is very high and cooling with the ethylene glycol-water mixture at operating point 8 is insufficient (IC2). In the experimental study conducted within the scope of this work, lines 6 and 7 were not activated because emergency operating conditions did not occur.

Mass balance equations:

$$\dot{m}_1 + \dot{m}_2 = \dot{m}_3 \tag{5}$$

$$\dot{m}_2 = \dot{V}_2 \overline{\rho}_2 M_{CH_4} \tag{6}$$

Where:

- $\dot{V}_2$ = the volumetric flow rate of fuel (m^3/s)
- $\overline{\rho}_2$ = the density of the gaseous fuel ($kmol/m^3$)
- M_{CH_4} = the molecular weight of the gaseous fuel (kg/kmol)

Energy balance equations:

The heat transfer from the internal combustion gas engine to intercooler 1 (IC1), $\dot{Q}_{IC1}$ can be expressed as

$$\dot{Q}_{IC1} = \dot{m}_8 C_{P_{EG}} (T_9 - T_8) \tag{7}$$

Where:

- $C_{P_{EG}}$ = specific heat of ethylene glycol-water mixture at constant pressure at average temperature (kJ/kg K)
- T = temperature (°C)

The total energy supplied to an internal combustion engine as a result of the combustion of natural gas is expressed by the following equation. In the calculations, methane (CH_4) will be used instead of natural gas because natural gas contains approximately 90% methane (Hoşgörmez *et al.* 2005).

$$\dot{Q}_{thv} = \overline{LHV}_{CH_4} \dot{V}_2 \overline{\rho}_2 \tag{8}$$

Where:

- $\dot{Q}_{thv}$ = the total heating value of the fuel as a result of the combustion of methane gas (kW)
- $\overline{LHV}_{CH_4}$ = the lower heating value of methane on a mole basis (kJ/kmol)

3.2. Heat Recovery System and Heat Exchangers

In the trigeneration system, as mentioned earlier, since the experiments are conducted during the winter months, the heat required to meet part of the electricity and building heating load is produced simultaneously. The heat transferred from the internal combustion gas engine to ethylene glycol in

IC1 is then transferred to the water circulating in pipelines 18 and 19 via the HTE, as schematically shown in Figure 6 below.

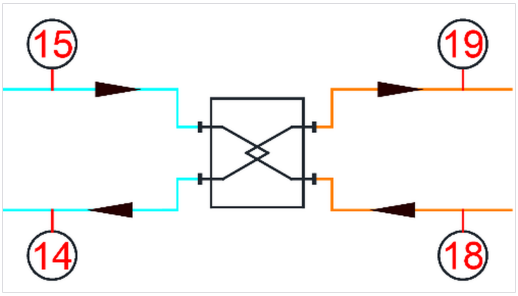

Figure 6. Illustration of a high-temperature heat exchanger (HTE).

The mass and energy equations for the HTE can be written as follows,

$$\dot{m}_{14} = \dot{m}_{15} = \dot{m}_8 = \dot{m}_9 \tag{9}$$

$$\dot{m}_{18} = \dot{m}_{19} \tag{10}$$

$$\dot{Q}_{HTEp} = \dot{m}_8(h_{EG,15} - h_{EG,14}) \tag{11}$$

$$\dot{Q}_{HTEp} = \dot{m}_{18}(h_{19} - h_{20}) \tag{12}$$

The water, having absorbed heat from ethylene glycol in the HTE, enters the HRS, schematically shown in Figure 7, with an increased temperature.

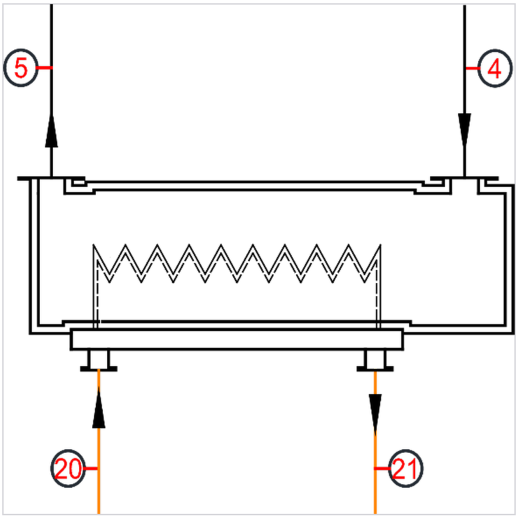

Figure 7. Heat recovery system.

Where:

- $\dot{Q}_{HTEp}$ = the primary heat transfer capacity of the HTE (kW)
- $\dot{Q}_{HTEs}$ = the secondary heat transfer capacity of the HTE (kW)
- EG = ethylene glycol

Waste heat from the exhaust gases entering the heat recovery system at point 4 and exiting at point 5 is transferred to the water entering at point 20 and exiting at point 21.

The mass and energy equations for the HRS can be written as follows,

$$\dot{m}_4 = \dot{m}_5 = \dot{m}_3 \tag{13}$$

$$\dot{m}_{20} = \dot{m}_{21} \tag{14}$$

$$\dot{Q}_{HRS} = \dot{m}_3 \left(\frac{\overline{h}_{EXG,4} - \overline{h}_{EXG,5}}{M_{EXG}} \right) \tag{15}$$

The volume fractions of the exhaust gases released as a result of the combustion of natural gas are given in Table 2.

Table 2. Volume fraction of exhaust gases (Bejan *et al.* 1996).

Exhaust gases	Volume fraction (%)
N_2	75.07
O_2	13.72
CO_2	3.14
$H_2O_{(g)}$	8.07

Where:

- EXG = exhaust gases
- $\dot{Q}_{HRS}$= the heat transferred by the exhaust gases to the heat recovery system (kW)
- M_{EXG} = the average molecular weight of the exhaust gases (kg/kmol)
- $\overline{h}_{EXG}$ = specific enthalpy of exhaust gases on a kilomole basis (kJ/kmol)

The volume ratios of exhaust gases given in Table 2 above are taken as the number of moles of exhaust gases. Then the molar ratios (y) of the exhaust gases are determined, and the enthalpy of the exhaust gases at the heat recovery inlet is calculated using the following equation.

$$\overline{h}_{EXG,4}(T_4) = \left[y_{N_2}\left(\Delta\overline{h}\right)_{N_2} + y_{O_2}\left(\Delta\overline{h}\right)_{O_2} + y_{CO_2}\left(\overline{h}^0_{f,CO_2} + \Delta\overline{h}\right)_{CO_2} + y_{H_2O(g)}\left(\overline{h}^0_{f,H_2O} + \Delta\overline{h}\right)_{H_2O(g)} \right](T_4) \tag{16}$$

$\Delta\overline{h}$ and $\overline{h}^0_f$ are taken from thermodynamic tables. The enthalpy at the heat recovery outlet ($\overline{h}_{EXG,5}(T_5)$) is calculated similarly.

Where:

- $\Delta\overline{h}$ = the enthalpy difference of the gases between the relevant temperature and the reference temperature (kJ/kmol)
- $\overline{h}^0_f$ = the enthalpy of formation of gaseous compounds (kJ/kmol)
- y = molar ratios (kmol/kmol)

The water, whose temperature has increased slightly in the HRS, finally reaches the HWE (Hot Water Heat Exchanger), where it transfers its heat to the water that meets a portion of the building's heating load, as shown in Figure 8.

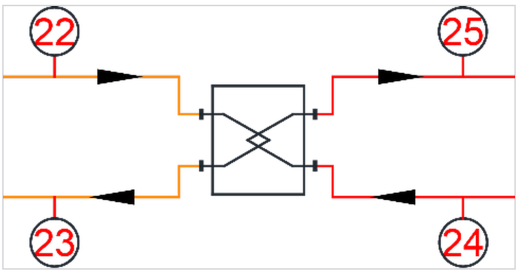

Figure 8. Representation of a hot water heat exchanger (HWE).

The mass and energy equations for the HWE can be written as follows.

$$\dot{m}_{22} = \dot{m}_{23} = \dot{m}_{20} = \dot{m}_8 \tag{17}$$

$$\dot{m}_{24} = \dot{m}_{25} \tag{18}$$

$$\dot{Q}_{HWEp} = \dot{m}_8(h_{22} - h_{23}) \tag{19}$$

$$\dot{Q}_{HWEs} = \dot{m}_{24}(h_{24} - h_{25}) \tag{20}$$

Where:

- $\dot{Q}_{HWEp}$ = the primary heat transfer capacity of the HWE (kW)
- $\dot{Q}_{HWEs}$ = the secondary heat transfer capacity of the HWE (kW)

The total heat energy $\dot{Q}_{th}$ produced by the internal combustion gas engine is the sum of the heat transferred to ethylene glycol in IC1 for cooling the internal combustion gas engine and the heat transferred by the exhaust gases to the heat recovery system.

$$\dot{Q}_{th} = \dot{Q}_{HRS} + \dot{Q}_{AC1} \tag{21}$$

The thermal efficiency of an internal combustion gas engine and generator set is expressed as follows:

$$\eta_{th} = \frac{\dot{Q}_{th}}{\dot{Q}_i} \tag{22}$$

$$\eta_{el} = \frac{\dot{W}_{el}}{\dot{Q}_i} \tag{23}$$

$$\eta_{tot} = \frac{\left(\dot{W}_{el} + \dot{Q}_{th}\right)}{\dot{Q}_i} \tag{24}$$

Where: η_{th} = the thermal efficiency of the motor-generator group

- η_{el} = the electrical efficiency of the motor-generator group
- η_{tot} = the total efficiency of the motor-generator group
- $\dot{W}_{el}$ = the electrical power produced by the motor-generator group. (kW)
- $\dot{Q}_{th}$ = the total heat energy produced by the internal combustion gas engine (kW)

4. Uncertainty Analysis of Experimental Measurements

Following the detailed methodology established by Holman (1984), the final experimental result R is determined as a function of n primary measured variables. Therefore,

$$R = R(x_1,\ x_2,\ x_3,\ \ldots,\ x_n) \tag{25}$$

Let Y_R denote the uncertainty associated with the final experimental result, while Y_1, Y_2,...,Y_n represent the uncertainties of the respective measured variables. In cases where all independent variable uncertainties are specified at an identical confidence level, the overall uncertainty in the experimental result is formulated by Holman (1984) as follows:

$$Y_R = \left[\left(\frac{\partial R}{\partial x_1} Y_1\right)^2 + \left(\frac{\partial R}{\partial x_2} Y_2\right)^2 + \left(\frac{\partial R}{\partial x_3} Y_3\right)^2 + \cdots + \left(\frac{\partial R}{\partial x_n} Y_n\right)^2\right]^{1/2} \tag{26}$$

The uncertainties of the measuring devices that are used to calculate the uncertainties are ± 1 m³/h for the ultrasonic mass flow meter, ± 3 % for the natural gas meter, ± 2.5 % for the Bourdon-type pressure gauge, and ± 1 % for the K-type thermocouple. The average parameter uncertainties are determined by EES (Klein 2020). The parameter uncertainties at the average outdoor air temperature are given in Table 3.

Table 3. The uncertainties at average air temperature in this experimental study.

Parameters	Average value of the parameter	Average uncertainties (%)
η_{tot}	84.79	0.46
$\dot{Q}_{thv}$	976.750 kW	0.12
$\dot{Q}_{IC1}$	199.217 kW	1.86
$\dot{Q}_{HTEp}$	194.681 kW	2.97
$\dot{Q}_{HTEs}$	187.428 kW	3.46
$\dot{Q}_{HWEp}$	936.383 kW	0.59
$\dot{Q}_{HWEs}$	371.417 kW	2.10
$\dot{Q}_{HRS}$	230.350 kW	0.04

5. Results and Discussion

The computer program incorporating the equations formulated within the thermodynamic model was developed using Engineering Equation Solver (EES) software. Average temperature, pressure, and flow rate data measured in experimental studies were entered into the developed computer program, and the results are presented graphically and discussed in detail in the following paragraphs.

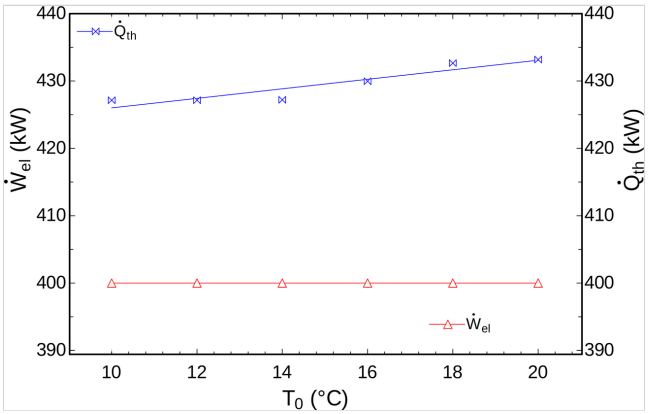

Figure 9. Variation of electrical power produced by the gas engine and total heat energy obtained from the gas engine as a function of outside air temperature.

Figure 9 shows the variation of electrical energy obtained from the generator driven by the gas engine and the heat energy provided by the engine as a function of the outside air temperature. As the outside air temperature increases, the electrical energy obtained from the generator remains unchanged, while the heat energy from the engine increases linearly.

Since the primary purpose of the trigeneration system in this facility is to provide electrical energy, the electrical devices powered by the system mustn't be damaged. Therefore, the system must provide a constant electrical energy output. For this reason, the system regulates the generated electrical energy by momentarily increasing or decreasing the gas flow rate, air-fuel mixture, pressure, outlet temperatures, etc. The generator, which produces the electricity, is located right next to the engine block and is driven by a short shaft. This configuration reduces losses in electricity production and makes it easier to control the electrical energy produced by the generator (in response to momentary changes in engine operation). As shown in Figure 9, this ensures that the system produces electricity consistently.

As shown in Figure 9, the thermal energy produced by the gas engine reaches its lowest value of 427.1 kW when the outside air temperature is 10 °C. At the same time, it reaches its highest value of 433.2 kW when the outside air temperature is 20 °C. The HRS unit transfers thermal energy from the engine jacket water to equipment such as heat exchangers via piping and uses it in the building. Heat energy is lost in much of the piping, equipment, and devices. For this reason, controlling thermal energy is more difficult than controlling electrical energy produced by the engine. Therefore, the thermal power of the gas engine increases by 6.1 kW depending on the outside air temperature. Considering that the manufacturer also designed the HTE capacity at 431 kW in the project design, this increase is very low, corresponding to 1.4% of the heat exchanger capacity.

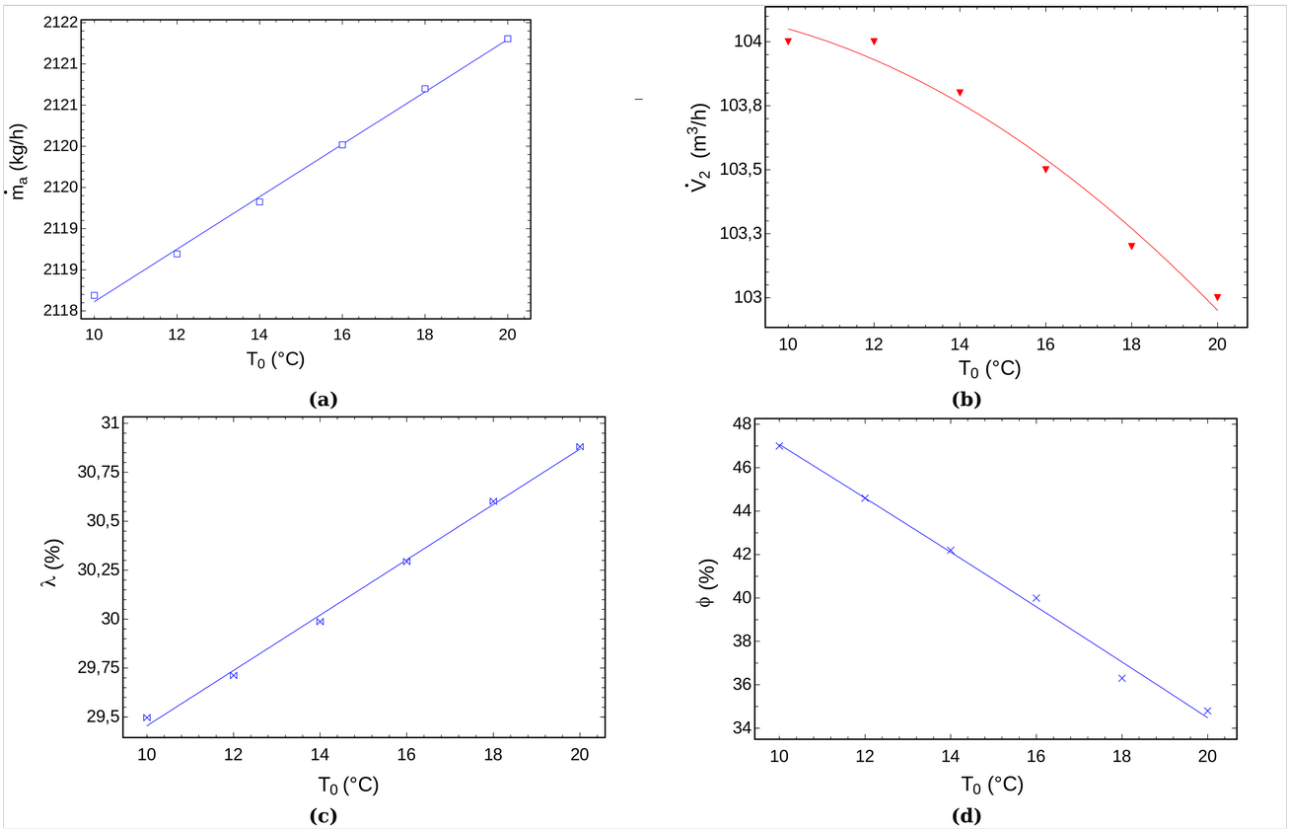

Figure 10. (a) Variation of air flow rate entering the gas engine, (b) Variation of fuel (natural gas) consumed by the engine, (c) Variation of air-fuel ratio, (d) Variation of humidity in the air, depending on the outside air temperature.

Figure 10 shows the variation of airflow into the engine, the amount of fuel consumed per unit time, the air-fuel ratio entering the engine, and the humidity in the air with respect to outside air temperature. In Figure 10 (a), the airflow entering the engine for combustion increased linearly by 0.1% from 2118 kg/h to 2121 kg/h as the outside air temperature changed from 10 to 20 °C. Figure 10(b) shows that fuel consumption decreased by 0.9% at the same outside air temperatures, decreasing parabolically from 104 m³/h to 103 m³/h. The change in combustion air entering the engine due to the increase in outside air temperature is adjusted more precisely and is 9 times smaller than the rate of change in engine fuel consumption. Figure 10(c) shows that the air-fuel ratio increased linearly by 1%, ranging from a low of 29.5% to a high of 30.5%, due to the proportional increase in outside air temperature. Figure 10(d) shows that the relative humidity of the air decreased gradually with increasing outside air temperature. Accordingly, the highest humidity level was measured at 47% when the air temperature was 10 °C, while the lowest humidity level was measured at 34.8% when the air temperature was 20 °C.

As is known, the compressor compresses the fuel-air mixture and sends it to the combustion chamber at a higher temperature and pressure. The temperature and moisture content of the fuel-air mixture in the combustion chamber are among the biggest factors affecting combustion. Since the intercooler keeps the fuel-air mixture at the optimum temperature, the air relative humidity affects the combustion reaction more than the air temperature. Under normal conditions, cylinder temperatures in gas engines are approximately 350–450 °C. These temperatures are continuously monitored by the SCADA automation system of the internal combustion gas engine. The amount of heat obtained from the fuel directly determines the cylinder temperatures. If the heat obtained from igniting the fuel-air mixture entering the cylinder is low, the air-fuel mixture ratio is adjusted using an inlet flap valve. According to the information received from the SCADA automation system, when the outside air temperature is low, the amount of fuel entering the engine is increased, and the

amount of air is reduced, resulting in rich combustion. As can be seen in Figure 10(b), when the outside air temperature increases, engine fuel consumption decreases. This is shown in Figure 10(c), where the air-fuel ratio gradually increases.

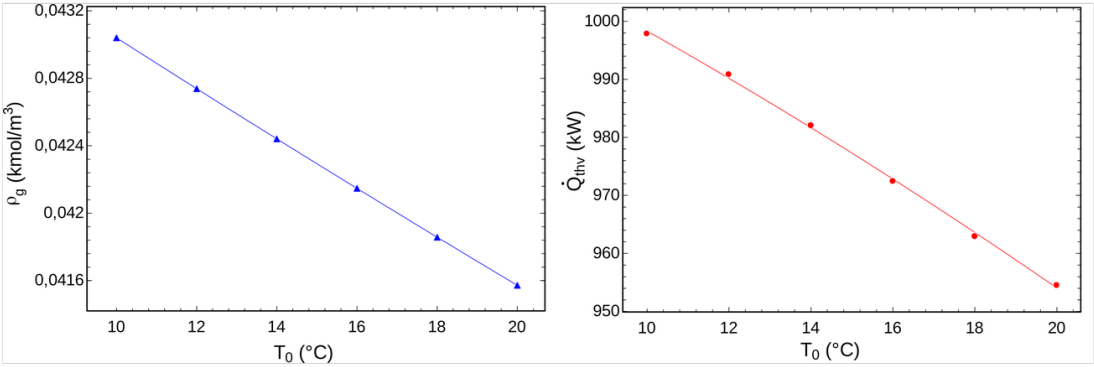

Figure 11. (a) Variation of fuel (natural gas) density entering the engine, (b) Variation of the total heating value of the fuel with respect to outside air temperature.

Figure 11 shows the variation of total heating value of the fuel and fuel density depending on the outside air temperature. In Figure 11(b), the thermal capacity peaks at 997.8 kW when the outside air temperature is 10 °C and decreases to 954.5 kW at 20 °C. Figure 11(a) shows that the density of natural gas entering the engine as fuel decreases linearly with the outside air temperature. According to the ideal gas law, gas density decreases as temperature increases at constant pressure. Accordingly, when the outside air temperature increases from 10 °C to 20 °C, the gas density decreases by 3.4%. The term "total heating value of the fuel" actually refers to the maximum heat output that can be obtained from a unit of fuel entering the engine. Since the total heating value of the fuel depends on the calorific value, density, and volume flow rate of the fuel, as seen in Figure 10(b), the mass flow rate of the gas (fuel) entering the engine decreased by 0.9%.

In comparison, its density decreased by 3.4% as the temperature increased. Consequently, the total heating value of the fuel also decreased. However, the main factor causing the greatest decrease in total heating value of the fuel was the decrease in gas density, which was 3.8 times greater than the decrease in flow rate.

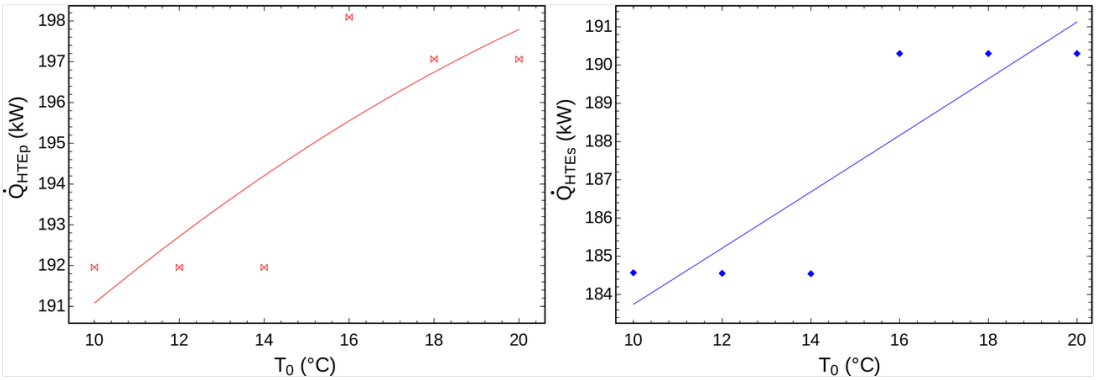

Figure 12. (a) HTE primary, (b) HTE secondary, variation of heat capacity with respect to outside air temperature.

Figure 12 shows the variation of the heat capacity of the HTE with respect to outside air temperature. As seen in Figure 12 (a), the heat capacity of the primary side of the HTE is a minimum of 192 kW at 10 °C for the outside air temperature range of 10 °C to 20 °C. As temperature increases, the heat capacity increases with a decreasing slope, reaching a maximum of 197 kW at 20 °C. As seen in Figure 12(b), the heat capacity of the secondary side of the HTE increases linearly from 184.5 kW at 10 °C to 190.3 kW at 20 °C for the outside air temperature range of 10 °C to 20 °C. The difference in heat

capacity between the primary and secondary sides of the HTE plate heat exchanger is 7.5 kW at 10 °C and 6.7 kW at 20 °C. This means that approximately 7.1 kW of heat is transferred from the HTE to the environment. The heat capacity of the HTE remained constant between 10 °C and 14 °C. Subsequently, as the engine block temperature increased, the heat capacity gradually increased as well. At 16 °C, due to the increased instantaneous heat transfer from the primary to the secondary side of the HTE, the primary heat capacity of the heat exchanger increased to 198 kW.

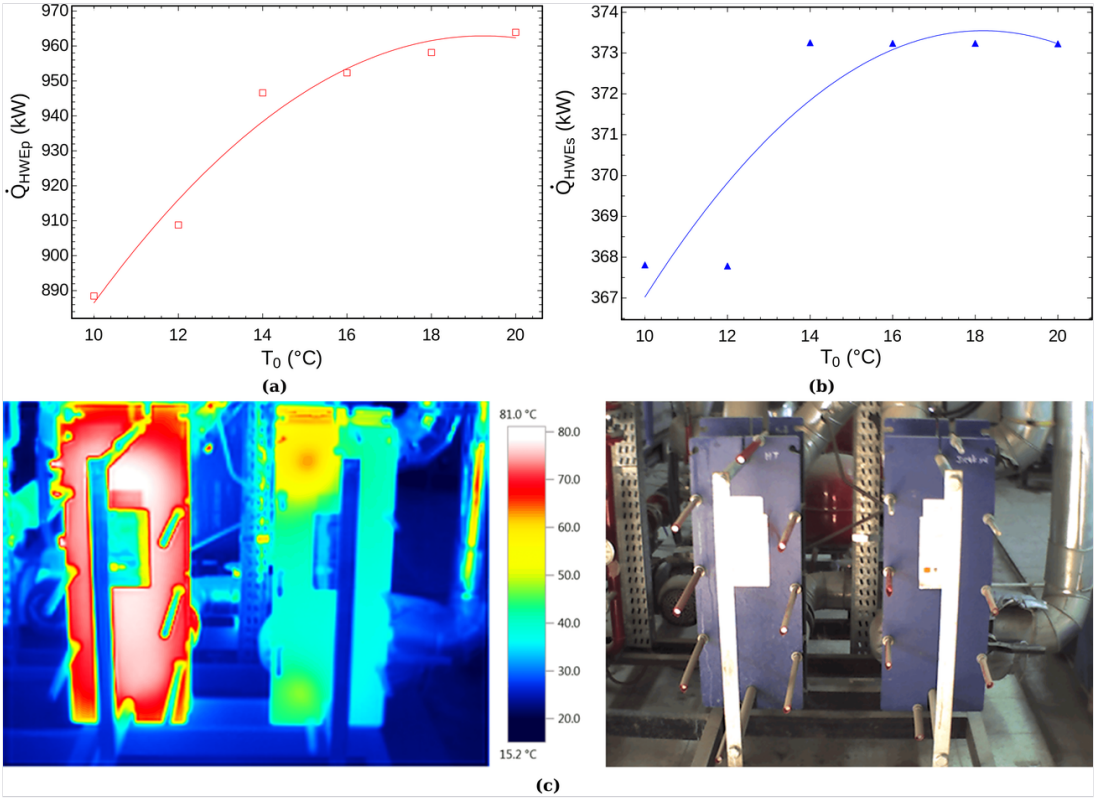

Figure 13. (a) Variation of heat capacities of HWE primary side, (b) HWE secondary side, with respect to outside air temperature, (c) Thermal camera image of HTE and HWE plate heat exchangers from left to right.

Figure 13 shows the variation of heat capacities in the primary and secondary sides of the HWE with outside air temperature. In theoretical studies, the capacities of the primary and secondary lines of plate heat exchangers are equal because ambient conditions are assumed to be isolated. However, in this case study, there are differences in the heat capacities calculated from inlet and outlet temperature measurements in the primary and secondary lines of plate heat exchangers, as shown in Figures 13(a) and 13(b). Insufficient heat exchanger surface area and inadequate insulation likely reduced the heat delivered to the secondary loop while increasing ambient heat losses, explaining the discrepancy between the primary and secondary heat transfer rates. As shown in Figure 13(a), when the outside air temperature is increased from 10 °C to 20 °C, the heat capacity of the primary side of the HWE increases linearly from 888.5 kW to 963.9 kW, an increase of approximately 8.5%. As seen in Figure 13(b), the heat capacity of the secondary line of the HWE increases with a decreasing slope of approximately 1.5% from 367.8 kW to 373.2 kW between 10 °C and 16 °C. It remains constant at 373.2 kW when the temperature increases from 18 °C to 20 °C. The thermal camera image in Figure 13(c) shows that the surface temperatures of the HTE are higher than those of the HWE. Although the HWE should normally operate at higher temperatures, it was cooler. This situation proves the case described above.

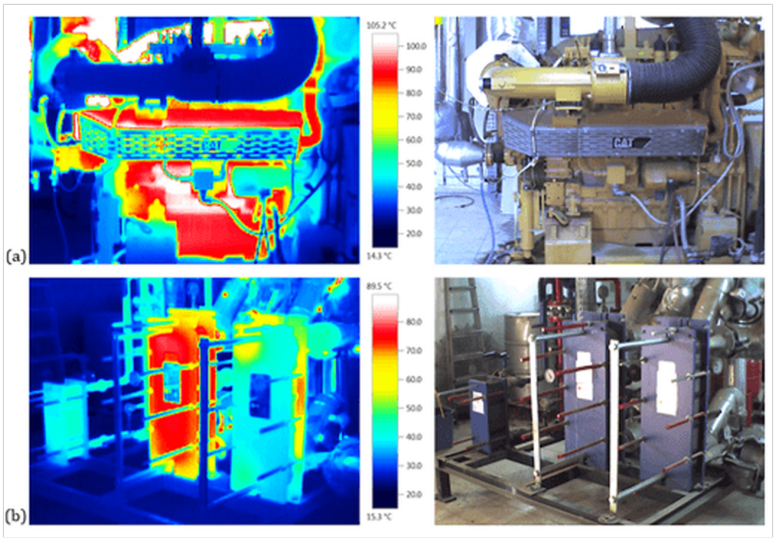

Figure 14. (a) Thermal camera view of the gas engine and (b) plate heat exchangers (LTE, HTE and HWE) respectively, from left to right.

In a trigeneration system, heat transfer occurs from the devices and equipment to the environment via radiation. This causes the indoor temperature of the facility to rise, hindering the efficient operation of the system. As shown in Figure 14, heat transfer occurs most frequently in the gas engine, followed by the SKID group (LTE, HTE, and HWE). When the gas engine was monitored with a thermal camera, the highest temperature measured on its outer surface was 107 °C (Figure 14(a)). According to the manufacturer's engine catalog value of the internal combustion gas engine used in the study, the heat radiated to the external environment during 100% capacity operation is approximately 33 kW. As previously explained for Figure 12, approximately 7.1 kW of heat is transferred from the HTE to the environment. The highest temperature measured on the HTE was 89.5 °C at the primary inlet line. In Figure 14, the amount of heat transferred from the HWE to the indoor environment is approximately 1.5 kW. The highest temperature measured on the HWE was 86.7 °C at the secondary outlet.

As shown in Figure 14(b), the greatest heat loss occurs in the HWE, while the least heat loss occurs in the LTE. Although the HWE heat capacity is much higher than that of other plate heat exchangers, the heat map temperatures in the HTE are higher. Because the flow in the HWE secondary line is 2.5 times higher than the designed flow rate, facilitating rapid heat transfer from the primary side to the secondary line. Therefore, although the HWE primary line operates at an average temperature of 90 °C to 60 °C, the secondary line operates at an average temperature of 45 °C to 38 °C.

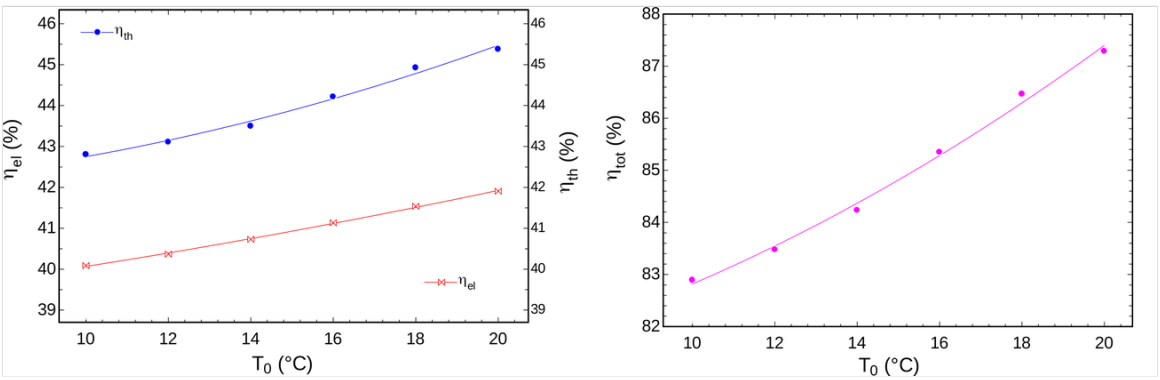

Figure 15. Variation of (a) electrical and thermal efficiency and (b) total efficiency of the gas engine with respect to outside air temperature.

Figure 15 shows the variation of the electrical, thermal, and total efficiencies of an internal combustion gas engine with respect to outside air temperature. As the outside air temperature increases, the engine's electrical efficiency increases from 40.09% to 41.91%, while the engine's thermal efficiency increases from 42.81% to 45.38%. The increase in electrical efficiency is linear, while the increase in thermal efficiency follows an upward slope compared to electrical efficiency. As previously mentioned, the electrical energy produced by the engine is constant. However, the main effect of increasing the engine's thermal and electrical efficiency is the gradual decrease in the engine's total thermal capacity. As seen in Figure 15(b), when the outside air temperature increases from 10 °C to 20 °C, the engine's total efficiency increases linearly by 4.4%, from 82.89% to 87.29%. According to the manufacturer's engine catalog information used in this case study, the engine's total efficiency is stated as 87.5% at 25 °C. Accordingly, increasing the outside air temperature from 20 °C to 25 °C allows the overall engine efficiency to be proportionally consistent with the engine catalog values.

6. Conclusion

The energy performance of the trigeneration system installed at Fatsa State Hospital was investigated for outdoor air temperatures ranging from 10 °C to 20 °C. In the present study, temperature, pressure, flow rate, and electrical power output were directly measured, while the other thermodynamic properties, energy quantities, and efficiency values were obtained from the developed thermodynamic model. The main findings are summarized as follows.

Experimental measurements showed that the electrical power output of the trigeneration system remained approximately constant at 400 kW as the outdoor air temperature increased from 10 °C to 20 °C. The measured temperature, pressure, and flow-rate data at the relevant operating points were used as input data for the developed thermodynamic model.

The measured volumetric flow rate of natural gas was 104 m^3/h at an outdoor air temperature of 16 °C and 103 m^3/h at 19 °C. Therefore, a slight decrease in the measured natural-gas flow rate was observed between these two operating conditions. According to the thermodynamic model calculations, the density of natural gas decreased with increasing outdoor air temperature. Consequently, the calculated volumetric heating value of the natural gas also decreased. This provides a possible thermodynamic explanation for the slight variation observed in the measured natural-gas flow rate.

The thermodynamic model predicted that increasing the outdoor air temperature from 10 °C to 20 °C increased the heat-transfer capacities of the HRS and HTE by 0.9 kW and 5.1 kW, respectively. The calculated heat capacity of the primary side of the HTE increased from 192 kW at 10 °C to 254 kW at 20 °C, whereas the calculated heat capacity of the secondary side decreased from 184.5 kW to 179 kW. According to the model, the difference between the heat capacities of the two sides indicates that the heat-transfer capacity of the secondary side limited the amount of heat transferred from the primary side.

The model calculations showed that the thermal power obtained from the internal combustion gas engine increased from 427.1 kW to 433.2 kW when the outdoor air temperature increased from 10 °C to 20 °C. Thus, the model predicted an increase of 6.1 kW in the recoverable thermal energy. This result should be regarded as a model-based prediction rather than a directly measured thermal output.

The energy efficiencies also increased with increasing outdoor air temperature. The electrical efficiency increased from 40.09% to 41.91%, while the thermal efficiency increased from 42.81% to 45.38%. Since the electrical power output was experimentally maintained at approximately 400 kW, the variation in calculated electrical efficiency resulted from the changes in the calculated energy input. The increase in calculated thermal efficiency was associated with the increase in the calculated thermal energy recovery capacity of the trigeneration system.

Declarations

Author contributions. Ali Kilicarslan: Conceptualization, Methodology, Investigation, Writing (review and editing), Writing (original draft), Supervision. Engin Sanli: Investigation, Formal analysis, Writing (original draft).

Funding. This research received no specific funding.

Conflicts of interest. The authors declare no competing interests.

Data availability. Not applicable. This study did not generate or analyse any datasets.

Acknowledgements. The authors would like to acknowledge the Scientific and Technological Research Council of Türkiye (TÜBİTAK-BİDEB) for their support under the '2224-A Grant Program for Participating in Scientific Activities Abroad (2026/1)' to present this paper at the 22nd International Conference on Sustainable Energy Technologies (SET2026), held in Kuala Lumpur, Malaysia, on August 13–15, 2026.

References

Alcântara, S.C.S.; Ochoa, A.A.V.; da Costa, J.A.P.; Michima, P.S.A.; Silva, H.C.N. (2019) 'Natural gas based trigeneration system proposal to an ice cream factory: An energetic and economic assessment', *Energy Conversion and Management*, 197, pp. 111860. Available at: https://doi.org/10.1016/j.enconman.2019.111860

Bejan, A.; Tsatsaronis, G.; Moran, M. (1996) *Thermal Design and Optimization*. John Wiley & Sons, New York.

Cavalcanti, Eduardo J.C. (2021) 'Energy, exergy and exergoenvironmental analyses on gas-diesel fuel marine engine used for trigeneration system', *Applied Thermal Engineering*, 184, pp. 116211. Available at: https://doi.org/10.1016/j.applthermaleng.2020.116211

Holman, J.P. (1984) *Experimental Methods for Engineers*. McGraw-Hill Book Company, USA.

Hoşgörmez, Hakan; Yalçın, M. Namık; Cramer, Bernhard; Gerling, Peter; Mann, Ulrich (2005) 'Molecular and isotopic composition of gas occurrences in the Thrace basin (Turkey): origin of the gases and characteristics of possible source rocks', *Chemical Geology*, 214(1-2), pp. 179-191. Available at: https://doi.org/10.1016/j.chemgeo.2004.09.004

Kaplan, Mehmet; Büker, Mahmut Sami (2019) 'Konutlarda paket tipi kojenerasyon ile yerinde enerji üretimi: Konya şartlarında uygulama', *Konya Journal of Engineering Sciences*, 7(4), pp. 749-767. Available at: https://doi.org/10.36306/konjes.654923

Klein, S.A. (2020) *Engineering Equation Solver (EES) (Academic Professional V10.836-3D)*. F-Chart Software. Available at: https://fchartsoftware.com

Luz-Silveira, J; Beyene, A; Leal, E.M; Santana, J.A; Okada, D (2002) 'Thermoeconomic analysis of a cogeneration system of a university campus', *Applied Thermal Engineering*, 22(13), pp. 1471-1483. Available at: https://doi.org/10.1016/s1359-4311(02)00064-9

Salem Szklo, Alexandre; Borghetti Soares, Jeferson; Tiomno Tolmasquim, Maurício (2004) 'Energy consumption indicators and CHP technical potential in the Brazilian hospital sector', *Energy Conversion and Management*, 45(13-14), pp. 2075-2091. Available at: https://doi.org/10.1016/j.enconman.2003.10.019

Sanli, E. (2022) *Energy and exergy analyses of a trigeneration facility with respect to real-time data*. M.Sc. thesis, Hitit University, Graduate School, Türkiye.

Santiago, Thalyta S.A.; Achiles, Ana Elisa; Dangelo, José Vicente H. (2022) 'Thermodynamic performance analysis and optimization of a trigeneration system with different configurations applied to a medium-sized hospital', *Energy*, 239, pp. 122195. Available at: https://doi.org/10.1016/j.energy.2021.122195

Shelar, Mahesh. N.; Bagade, S.D.; Kulkarni, G.N. (2016) 'Energy and Exergy Analysis of Diesel Engine Powered Trigeneration Systems', *Energy Procedia*, 90, pp. 27-37. Available at: https://doi.org/10.1016/j.egypro.2016.11.167

Üçgül, İ.; Elibüyük, U. (2015) 'Üniversite yerleşkeleri için doğalgazlı trijenerasyon sisteminin değerlendirilmesi', *Mühendislik Bilimleri ve Tasarım Dergisi*, 3(2), pp. 105-109.

Ziher, D.; Poredos, A. (2006) 'Economics of a trigeneration system in a hospital', *Applied Thermal Engineering*, 26(7), pp. 680-687. Available at: https://doi.org/10.1016/j.applthermaleng.2005.09.007

HOW TO CITE THIS PAPER

Kilicarslan, A. and Sanli, E. (2026). Experimental energy analysis of a trigeneration system based on outdoor air temperature: a case study at Fatsa State Hospital, Türkiye. In: *Proceedings of the 22nd International Conference on Sustainable Energy Technologies (SET2026)*, Kuala Lumpur, Malaysia, 13 to 15 August 2026. Caravel Press, pp. 49–68. ISBN 978-1-995850-00-9. ISSN 2978-4387. https://doi.org/10.65582/set.2026.005

COPYRIGHT AND LICENCE

© 2026 The Author(s). This is an open access paper distributed under the terms of the Creative Commons Attribution (CC BY 4.0) licence, which permits unrestricted use, distribution and reproduction in any medium, provided the original work is properly cited.

WSSET World Society of Sustainable Energy Technologies Organised by the World Society of Sustainable Energy Technologies. Published by Caravel Press.